The damping influence in monitoring the tension of cable using the vibration method

An Huynh-Thai, Toan Pham-Bao*, Luan Vuong-Cong
Laboratory of Applied Mechanics (LAM), Ho Chi Minh City University of Technology (HCMUT), VNU-HCM, Vietnam.
htan.sdh232@hcmut.edu.vn, http://orcid.org/0000-0003-1436-4932
baotoanbk@hcmut.edu.vn, http://orcid.org/0000-0002-2105-2403
vuongluan@hcmut.edu.vn , http://orcid.org/0000-0003-4146-9297

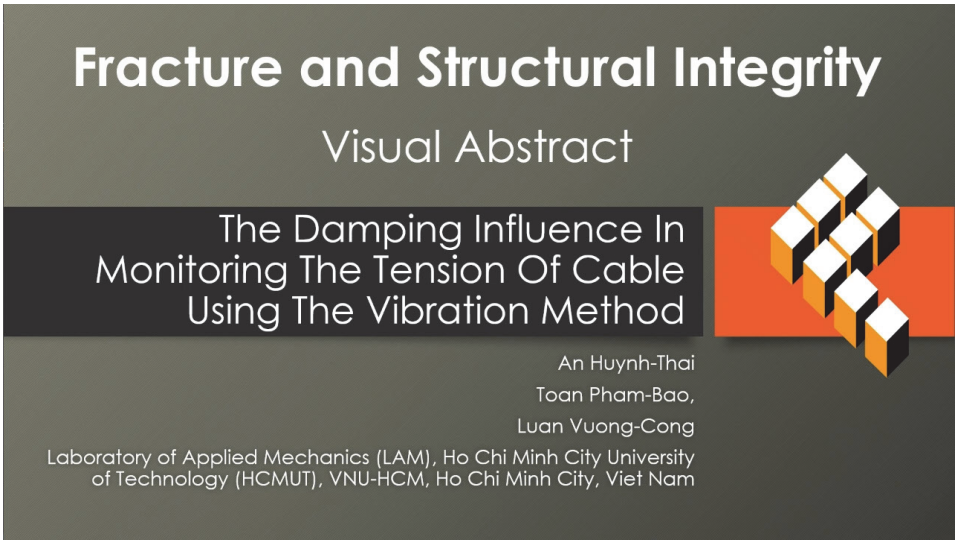

Citation: Huynh-Thai, A., Pham-Bao, T., Vuong-Cong, L., The damping influence in monitoring the tension of cable using the vibration method, Fracture and Structural Integrity, 76 (2026) 99-116.

Received: 16.10.2025
Accepted: 12.01.2026
Published: 22.01.2026
Issue: 04.2026

KEYWORDS. Rayleigh beam, Vibration, Cable, Damping, Viscoelastic.

INTRODUCTION

Cable vibration regularly occurs in operating structures and negatively impacts the performance and long-term maintenance of cable-supported structures. Therefore, it is necessary to develop solutions to control and predict the condition of structures, especially cable structures such as stayed cables of cable-stayed bridges, suspenders of suspension bridges, and hangers of arch bridges. Pre-stressed or stayed cables typically consist of steel wire bundles (near-linear elasticity), a corrosion-resistant high-density polyethylene (HDPE) jacket, protective grease or cement mortar, anchorage assemblies, and sometimes viscoelastic damping. Therefore, the observed damping of vibrations is not only due to the steel but also to the polymer components and the contact surfaces. In terms of material mechanics, this can be modeled in various ways. Steel has low but non-zero internal friction; in addition, fiber friction, anchor slippage, and mortar micro-cracking contribute to the structural damping, along with polymers (HDPE, sealants, and anchor pads). When inspecting cable structures, estimating the tension acting on the cable based on the vibration technique plays a significant role, due to the damping effect of cables. Vibration measurement using accelerometers is more commonly employed in

buildings due to its flexible implementation at a low cost, while ensuring good accuracy and meeting construction safety standards. Therefore, practical formulas are proposed to improve the accuracy of determining cable tension for different cable structures, without considering damping. For basic cable systems, damping is typically negligible and may be ignored, allowing accurate tension estimation from natural frequencies alone. In contrast, special cable types such as stay cables often incorporate multiple layers of steel wire bundles (exhibiting near-linear elasticity), as well as corrosion-resistant HDPE jackets. The presence of polymer components and friction at contact surfaces introduces significant damping behavior, which must be considered for reliable cable tension estimation. Owing to the damping of cable material, estimating the tension based on the vibration technique plays a significant role.

To enhance the accuracy of methods for determining cable strength using the vibration method, numerous scientists have researched and refined their techniques for evaluating cable tensile force. Shimada et al. propose a practical workflow: preferably, measure multiple natural frequencies; shape modes and correct for boundary conditions; estimate tensile force with optional adjustment via multi-mode regression; and cross-validate across modes and time [1]. The main advantages include higher accuracy compared to using the first mode, reduced reliance on direct measurements, and enhanced suitability for structural health monitoring (SHM) of stay cables and suspension cables. However, several critical factors must be addressed to ensure reliable field deployment: mode identification, temperature, cable deflection, boundary condition, and sensor calibration [2]. Tabatabai et al. focused on assessing the condition of stay cables using vibration measurement techniques. Instead of relying solely on visual inspection or traditional load testing methods, this study exploits the vibrational behavior of cables to detect changes in tensile force, stiffness, or potential damage. This method offers advantages of feasibility, low cost, and continuous monitoring, thereby supporting maintenance, ensuring safety, and extending the service life of modern cable-stayed bridges [3]. Cho et al. conducted a field study to compare methods for measuring cable tension in cable-stayed bridges. By applying various techniques, the authors evaluated the accuracy, feasibility, and limitations of each method under real-world conditions. They selected suitable measurement solutions for monitoring and maintenance work, thereby enhancing the reliability and safety of the cable system [4]. Two popular methods (the lift-off method and the vibration method) were compared and evaluated for determining bridge cable tension [5]. The research results not only contribute to improving the reliability of monitoring and maintenance of cable-stayed bridges but also have practical significance for transport infrastructure. In 2017, Jakiel and Manko developed a method for estimating the tension in cable-stayed pedestrian bridges based on measurements of natural frequencies. Through the analysis of experimental vibrations, the authors have developed a computational model that enables the indirect yet effective determination of cable tension, thereby replacing the complex and expensive direct measurement methods for wide application in structural health monitoring and the maintenance of cable-stayed bridges [6]. Suangga et al. focused on determining the tensile force in cable-stayed bridges through the analysis of natural frequencies. The authors conducted experimental measurements and compared them with theoretical models, thereby demonstrating that exploiting the relationship between frequency and cable tension is an effective, minimally invasive, and applicable method for SHM [7]. In 2023, Syamsi et al. investigated the impact of the location of the first sensor relative to the support on determining the tensile force of a cable with two fixed ends. By using a multi-sensor synchronized vibration measurement system, the authors analyzed how this distance change affects the accuracy of the tension estimation results. The results showed that selecting a reasonable sensor location plays a crucial role in reducing errors and enhancing the reliability of the vibration measurement method [8]. Kosco et al. (2024) focused on the development and application of the vibration method to estimate cable tension in cable-stayed and suspension bridges, thereby contributing to the improvement of safety and longevity for the project [9]. However, the similarity among the above studies lies in modeling the cable as an Euler-Bernoulli beam with an axial force and determining the relationship between the undamped vibration of the beam and the cable tension.

In another aspect, some researchers have expanded the beam theory to incorporate different mechanical characteristics, such as the Euler-Bernoulli, Rayleigh, Timoshenko, and Rayleigh-Love models, highlighting the differences in frequency and mode shape, as well as the range of their applications. Ignoring the role of rotational inertia and shear deformation can cause significant errors, especially for short beams or high-frequency vibrations; thus, advanced models such as Rayleigh or Timoshenko are often necessary to predict the dynamic response more accurately [10] [11]. Nathaniel and Alimi researched the dynamic behavior of a uniform Rayleigh beam subjected to an accelerated mass along its length. Instead of considering only static or moving loads with constant velocity, this study extended the analysis to the case of an accelerating mass, thereby clarifying the influence of rotational inertia and shear deformation on the vibration response [12]. Yang et al. (2018) developed an analytical model to analyze the material damping behavior of carbon fiber reinforced composite (CFRP) cantilever beams in the low-frequency domain. The study focused on describing the influence of composite material structure and energy dissipation mechanisms on vibration response, thereby providing a more accurate prediction tool than traditional models [13]. Zhu and Chung (2019) developed a Rayleigh model for a double-support beam that accounts for both longitudinal and rotational motion. The model was dimensionless and discretized using the Galerkin method with

eigenfunctions of sinusoids to obtain the mass, gyro, and stiffness matrices for natural frequencies and responses [14]. Moreover, the damping part is specially studied as viscoelastic damping using Kelvin-Voigt models or the Zener model, and then expanded upon with a fractional derivative. Rossikhin and Shitikova researched the development and application of the fractional Kelvin-Voigt model in describing the viscoelastic behavior of materials. Through theoretical analysis and simulation, the authors demonstrate that the introduction of the fractional derivative helps the model to more accurately reflect the time-dependent degradation and deformation characteristics, which cannot be fully described by the classical model [15]. Xu et al. proposed a new method for monitoring cable tension in cable bridges by using multiple sensors to identify mode shapes and boundary conditions via a Bernoulli-Euler model with linear/rotational springs. Field tests on a three-span arch bridge in China achieved <3% error, far better than beam theory and comparable to the flux method, confirming accuracy and cost-effectiveness [16]. Khang et al. (2021) investigated the forced transverse vibration of Euler-Bernoulli beams with fractional viscoelasticity using the modal analysis method. Instead of using the classical linear elastic model, the author introduced the fractional operator to describe the material's complex viscoelastic properties more accurately, thereby constructing an analytical solution for the forced vibration response. The results demonstrate that the fractional model can more accurately reflect the actual dynamic behavior of the beam, particularly in cases where the traditional model is no longer applicable [17]. Łabędzki researched the application of the fractional Kelvin-Voigt model for beam vibration analysis by numerical analysis.

Additionally, the study proposed a method to approximate the fractional model using the classical model in some instances, thereby making it more convenient for practical applications. This study contributes to strengthening the role of fractional analysis in modern structural mechanics and vibration analysis [18]. Combining these studies, scientists have investigated cables modeled as beams, such as in the contemporary landscape of cable tension estimation and vibration control, which is moving toward field-robust tools. Le et al. performed artificial neural network models trained on simulations to infer tension under limited prior data, with full-scale validation [19]. Furukawa (2023) introduces a natural frequency approach that jointly identifies tensile force, bending stiffness, and damper parameters for damped cables; subsequently. Then, damper-model dependence was removed via a mode-shape-based estimator to study, achieving an experimental error of ≤4% and outperforming design-formula methods [20] [21]. Nguyen (2024) formulates the combined action of viscous and HDR dampers, revealing near-additive damping and the governing role of damper-support flexibility. Overall trends favor multi-mode measurements, machine learning, and shape information to reduce modeling bias and optimize damper layouts for accurate, cost-effective SHM. Remaining gaps include field standardization, sensitivity to complex boundary conditions, and long-term calibration needs [22].

In this research, a cable has been modeled as an axially loaded Rayleigh beam, assuming the fractional derivative Kelvin-Voigt damping model from viscoelastic properties. A tensile force has been applied to the cable under supported conditions at both ends. Some applied calculations were conducted and compared to enhance the procedure for evaluating the tensile force of cables and cable structures, taking into account the damping material.

METHODOLOGY

Under working conditions, the tensile cables are influenced by the effect of the excited environment, which leads to vibration for the cable structure. Their known reaction is the creation of mechanical phenomena such as tensile force, flexural rigidity, damping effects, and rotatory inertia, as shown in Figure 1.

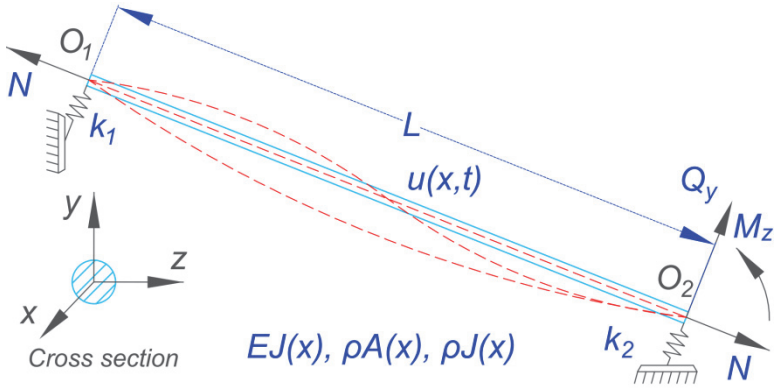

Figure 1: Mechanics diagram of the viscoelastic material cable.

In this study, the inertia due to the axial displacement of the beam included in the Rayleigh beam, as known rotatory inertia, $\rho J(x)$, is considered to have a damping effect γ(x). This is because, under the plane cross-section assumption, the axial displacements of points within a given cross section are equivalent to a rigid-body rotation about the z-axis, associated with the sectional moment of inertia $\rho A(x)$, flexural rigidity $EJ(x)$, cable length, L, axial tensile force, $N(x)$, and the dynamic excited load of $f(x,t)$ per unit length [12]. A general partial differential equation (PDE) for a vibrating cable, $u(x,t)$, is the equation of transverse motion, which has been modeled as a Rayleigh beam with tensile force and damping property of its material [14]. In this study, the fractional derivative Kelvin-Voigt model has been used to assess the damping influence on the tensile force of cables by extending the classical Kelvin-Voigt model with by a^{th} order fractional derivative with $0<\alpha<1$, as shown in Eqn. (1) [15].

$$\gamma(x) = \mathrm{C}_{\alpha}\partial_t^{\alpha} J\frac{\partial^2 u(x,t)}{\partial x^2} \tag{1}$$

where: C_a is the viscoelastic damping coefficient per unit length (with units of Pa.s$^{\alpha}$), obtained through cross-sectional integration, which depends on the excitation frequency as well as the viscoelastic properties of the material. The parameter a is a dimensionless fractional order, and ∂_t^{α} denotes the Riemann–Liouville fractional derivative of order α. [23]. Additionally, the fractional derivatives effectively specialize energy propagation and memory effects of viscoelastic materials [18].

For this study, considering free vibration and homogeneous, uniform cross-sections of cable do not change, which lead to ring down artifact $f(x,t)= 0$, properties of material from the governing differential equation for the cable vibration as E, J, ρ, and A are clearly assumed as constants per unit of length as Eqn. (2) [12]:

$$\mathrm{E}J\frac{\partial^4 u(x,t)}{\partial x^4} + \gamma(x)\frac{\partial^2 u(x,t)}{\partial x^2} - N\frac{\partial^2 u(x,t)}{\partial t^2} + \rho A\frac{\partial^2 u(x,t)}{\partial t^2} - \rho J\frac{\partial^4 u(x,t)}{\partial x^2 \partial t^2} = 0 \tag{2}$$

According to the expansion theorem, any function that satisfies the boundary conditions of the beam denotes a possible transverse displacement of the beam can be expressed as a sum of eigenfunction [17] as:

$$u(x,t) = \sum_{k=1}^{\infty} W_k(x)T_k(t) = \sum_{k} W_k(x)De^{\pm i\omega t} \tag{3}$$

$$W(x) = \sum_{k=1}^{\infty} C_k e^{is_k x} = C_1 sins_1 x + C_2 coss_2 x + C_3 sinhs_3 x + C_4 coshs_4 x \tag{4}$$

$$\mathrm{E}^* J\mathrm{W}^{(4)}(x)\mathrm{T}(t) - \mathrm{N}\mathrm{W}''(x)\mathrm{T}(t) + \varrho\mathrm{A}\mathrm{W}(\mathrm{x})\ddot{T}(t) - \varrho\mathrm{J}\,\mathrm{W}''(x)\ddot{T}(t) = 0 \tag{5}$$

In the time domain, the viscoelastic behavior of the cable material is described by a fractional Kelvin–Voigt constitutive relation, in which the stress is related to the strain through an elastic component and a Riemann–Liouville fractional derivative of order α acting on the strain field. To solve the governing equation, the method of separation of variables is applied, and the transverse displacement $u(x,t)$ is expressed as the product of a spatial mode shape $W(x)$ and a time-dependent response function T(t). By applying the Fourier transform to the fractional Kelvin–Voigt constitutive relation, the formulation is transferred from the time domain to the frequency domain. In this study, the Riemann–Liouville fractional derivative of order α acting on the strain field is represented by the factor $(i\omega)^{\alpha}$ [17, 24]. With $T(t)=De^{\pm i\omega t}$ as given in Eqn. (3), substituting the effective complex modulus of the viscoelastic material $E^*(\omega)=E+C_a\partial_t^{\alpha}=E+C_a(i\omega)^a$ into Eqn. (5) yields the spatial differential equation given in Eqn. (6). Consequently, the characteristic equation of the system is obtained in Eqn. (7).

$$\mathrm{E}^* \mathrm{J}\,\mathrm{W}^{(4)} + \left(\varrho\mathrm{J}\omega^2 - \mathrm{N}\right)\mathrm{W}'' - \varrho\mathrm{A}\,\omega^2\mathrm{W} = 0 \tag{6}$$

$$E^{*}Js^{4}+\left(\varrho J\omega^{2}-N\right)s^{2}-\varrho A\omega^{2}=0 \tag{7}$$

The solutions of Eqn. (7) are given by:

$$s^{2}=\pm\frac{-\left(\varrho J\omega^{2}-N\right)\pm\sqrt{\left(\left(\varrho J\omega^{2}-N\right)\right)^{2}+4E^{*}J\varrho A\omega^{2}}}{2E^{*}J} \tag{8}$$

In this study, the cable ends are modeled as elastic support boundary conditions by applying stiffness values (like springs) denoted by k_1 and k_2, respectively.

$$\frac{\partial}{\partial x}\left(EJ\frac{\partial^{2}u(x,t)}{\partial x^{2}}\right)\pm C_{\alpha}J\frac{\partial^{\alpha}}{\partial t^{\alpha}}\left(\frac{\partial^{2}u(x,t)}{\partial x^{2}}\right)\pm k_{n}u(x,t)\pm\varrho A\frac{\partial^{2}u(x,t)}{\partial t^{2}}=0\ \ with\ x=0\ or\ L \tag{9}$$

where: k_n denotes the spring stiffness, with k_1 at left end ($x=0$) and k_2 at the right one ($x=L$), see Fig. 1. In this case, the bending moment at both ends is zero.

$$EJ\frac{\partial^{2}u(x,t)}{\partial x^{2}}=0\ \ with\ x=0\ or\ L \tag{10}$$

If the boundary condition of both cable ends is simply supported [20], the viscoelastic damping coefficient is determined as follows

$$C_{\alpha}=\frac{\eta E}{(2\pi f)^{\alpha}\left(sin\frac{\alpha\pi}{2}-\eta cos\frac{\alpha\pi}{2}\right)} \tag{11}$$

Complex modulus shall be rewritten [13] [14] as:

$$E^{*}(\omega)=E+C_{\alpha}(i\omega)^{\alpha}=E'+E'' \tag{12}$$

The storage modulus (E'), the real part of Eqn. (12), is directly measured from vibration signal, and the dissipative modulus (E'') which is the imaginary part, is indirectly determined as shown in Eqns. (13) and (14) [15].

$$E'=Re\left(E^{*}(\omega)\right)=E+C_{\alpha}\omega^{\alpha}\cos(\alpha\pi/2) \tag{13}$$

$$E''=Im\left(E^{*}(\omega)\right)=C_{\alpha}\omega^{\alpha}\sin(\alpha\pi/2) \tag{14}$$

And the loss factor from cable material is also a function of frequency is derived:

$$\eta(\omega)=\frac{E''}{E'}=\frac{C_{\alpha}\omega^{\alpha}\sin(\alpha\pi/2)}{E+C_{\alpha}\omega^{\alpha}\cos(\alpha\pi/2)} \tag{15}$$

The spatial modes remain unchanged because the damping component only affects the frequency domain. For a nontrivial solution of C_2 and C_4 in boundary conditions, the determinant of their coefficient matrix is set equal to zero. Consequently, Eqn. (16) is obtained as follows:

$$N = \frac{4\pi^2 f^2 \left(\rho A + \rho J \beta_n\right) - \left(\mathrm{E} + \mathrm{C}_\alpha (\mathrm{i}\omega)^\alpha\right) J \beta_n^4}{\beta_n^2} \tag{16}$$

$$\beta_n \approx \frac{n\pi}{L + \frac{\mathrm{E}^* J}{k_1} + \frac{\mathrm{E}^* J}{k_2}} \tag{17}$$

where: β_n is the parameter depends on boundary conditions, k_1 and k_2 are the stiffness of spring, n is the number of modes. In small damping case, approximation for expressions $C_\alpha\omega^\alpha << E$ and $\eta \approx (C_\alpha/E\omega^\alpha \sin(\alpha\pi/2)$ [15]. The fractional exponent α with range from zero to one governs the nature of the viscoelastic response. When α is equal one, the model reduces to the classical Kelvin–Voigt formulation, in which the damping term is linear in velocity and the effective loss factor is given by $\eta = \omega C/E$, where ω is the angular frequency, C is the fractional damping coefficient, and E is the elastic modulus. Conversely, when α is equal zero, the damping term vanishes and the material tends toward purely elastic behavior without energy dissipation. This illustrates the essential role of α in modulating energy dissipation and intrinsic material damping.

In this study, the hierarchical Bayesian model [25] is employed to estimate the viscoelastic parameter vector of each cable, X=(E',Cα,f,η), which governs the fractional Kelvin–Voigt behavior. The physical constitutive relation is expressed through the complex modulus in Eqn. (12), from which the storage and loss components are derived, providing direct insight into the elastic and dissipative characteristics of the cable material. To represent variability across different cables, hierarchical priors are assigned to the parameters E', C_α, f, η enabling the model to separate true material variability from segment-level estimation noise.

At the segment level, the parameters (a, b) or their corresponding empirical forms are characterized using statistical descriptors such as means μa, μb and their associated standard deviations μ_{sd}^a, μ_{sd}^b. For each segment, the parameters (a, b) are obtained via a local optimization step, and the Hessian matrix at the optimum is used to quantify identification confidence, expressed through μ_{sd}^a and μ_{sd}^b. These segment-wise parameter distributions are then fused within the hierarchical structure, yielding global hyper-parameter estimates and corresponding 99% credible intervals (CI99), such as ${}_a\mu_{CI99}^{low} - {}_a\mu_{CI99}^{high}$ and ${}_b\mu_{CI99}^{low} - {}_b\mu_{CI99}^{high}$ [25]. The modeling or measurement uncertainty is described by the mean σ, its standard deviation σsd, and the 99% credible bounds ${}_\sigma\mu_{CI99}^{low} - {}_\sigma\mu_{CI99}^{high}$, while N_{obs}, reports the number of data points supporting each model. Local parameter estimation relies on numerical optimization, and the Hessian at the optimum provides a Gaussian approximation for quantifying local uncertainty.

At the hierarchical level, information from all cables and segments is fused to infer the hyper-parameters, which encode the population-level distribution and inter-cable variability. The joint posterior is explored using Markov Chain Monte Carlo (MCMC), enabling full posterior characterization, convergence diagnostics, and uncertainty propagation for cable-tension prediction. Parameter identifiability such as parameter collinearity or non-uniqueness under certain excitation spectra are examined, and prior sensitivity analyses are conducted to ensure robustness of the inferences.

This hierarchical Bayesian framework provides reliable viscoelastic parameter estimates for each cable and enables probabilistic prediction of cable tension, explicitly distinguishing physical variability from modeling and measurement uncertainty.

In the next section, the vibration data measured at cables of the Hwamung bridge (Busan city) [4] during construction were used to validate the damped vibration model of this study. Then, cable vibration of Phu My Cable-Stayed Bridge (Ho Chi Minh city) were used to investigate tension considering damping with proposed model.

VALIDATION AND TEST

Validation

In this research, the proposed method is applied and validated by Choi's data [4], which were collected from the Hwamung bridge, Korea. The cable properties and geometry for BLC02 cable of the Hwamung bridge are shown in Tab. 1, the first six frequencies are shown in Tab. 2, and Tab. 3 will show the comparison of other methods with this study's method.

Properties		BLC02
Number of strands		49
Length	m	45.568
Mass	kg/m	66.189
Modulus	Pa	1.95×10^{11}
Area moment of inertia	mm^4	2.37×10^{-5}
Area	mm^2	7350

Table 1: The properties of test cables of the Hwamyung bridge [4].

Phase	Cable Frequency (*Hz*)					
	First	Second	Third	Fourth	Fifth	Sixth
Before first tensioning	2.600	5.115	7.605	10.242	13.001	15.564
After first tensioning	2.576	5.054	7.495	10.120	12.744	15.320
Before second tensioning	2.557	4.987	7.477	9.961	12.433	15.381
After second tensioning	3.058	6.000	8.881	11.74	15.040	17.932
Finish of the second tensioning	3.058	6.030	9.021	11.871	15.064	17.993

Table 2: The measured frequency of BLC02 cables in Hwamyung cable-stayed bridge [4].

Phase	Tensile force (*kN*)						
	Design [4]	Taut string theory	Shimada's study [2]	Tabatabai's study [3]	This study α=0.1	This study α=0.001	This study α=0.00001
Before first tensioning	3273	3604 (10.12%)	3677 (12.34%)	3546 (8.34%)	3198 (2.29%)	3218 (1.67%)	3192 (2.45%)
After first tensioning	3162	3526 (11.53%)	3555 (12.43%)	3448 (9.06%)	3113 (1.55%)	3133 (0.91%)	3107 (1.71%)
Before second tensioning	3057	3459 (13.15%)	3497 (14.40%)	3380 (10.59%)	3058 (0.06%)	3079 (0.72%)	3053 (0.11%)
After second tensioning	4789	4480 (6.43%)	4883 (1.98%)	4792 (0.08%)	4551 (4.95%)	4572 (4.53%)	4546 (5.06%)
Finish of the second tensioning	4704	5036 (7.07%)	4929 (4.79%)	4846 (3.03%)	4619 (1.81%)	4639 (1.37%)	4614 (1.91%)

(·) denote the error of tension by vibration based methods compared to design values.

Table 3: Comparison of the tensile force with the value from formulas of previous studies [4].

The proposed model with linear spring at each end is well suitable, as the error is less than 4.71% with $\alpha\approx0.001$. In the next subsection, calculations for a real measurement were conducted for collected data at Phu My bridge.

Real data from measurement

In 2017, some measuring trips with ten sessions for each measuring trip was performed for some cables in the Phu My bridge, a cable-stayed bridge crossing the Sai Gon River (Fig. 2). Tab. 4 shows cable properties and geometry for measured cables labeled C2102N, C2207N, C2212N, C2215N, and C2115N. The measured data which shall be processed by the Fourier transform (Fig. 3) to determine the tensile force, have collected about 270 frequency data with some missing data due to noise or error.

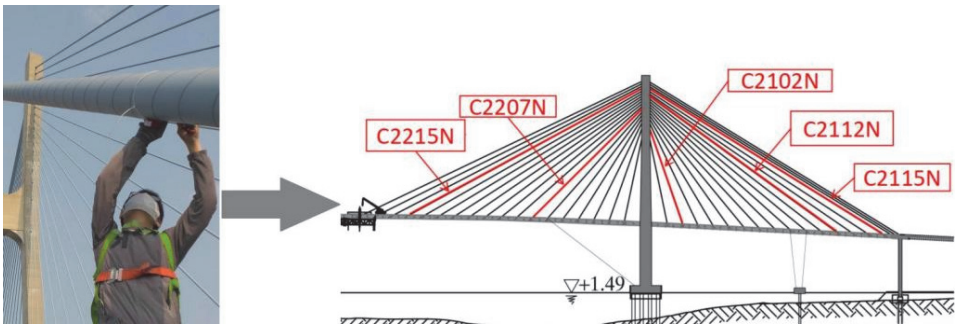

Figure 2: The measuring trip at Phu My bridge.

Properties		Multistrand Cables				
		C2102N	C2115N	C2207N	C2112N	C2215N
Number of strands		27	51	35	45	51
Length	m	68.133	55.917	101.219	148.124	179.223
Mass	kg/m	31.86	60.189	41.3	53.1	60.18
Modulus	Pa	1.97×10^{11}	1.97×10^{11}	1.97×10^{11}	1.97×10^{11}	1.97×10^{11}
Area moment of inertia	mm^4	8.36×10^{-6}	2.37×10^{-5}	1.37×10^{-5}	2.18×10^{-5}	2.47×10^{-5}
Area	mm^2	4050	7650	5250	6750	7650

Table 4: The properties of five cables of the Phu My bridge.

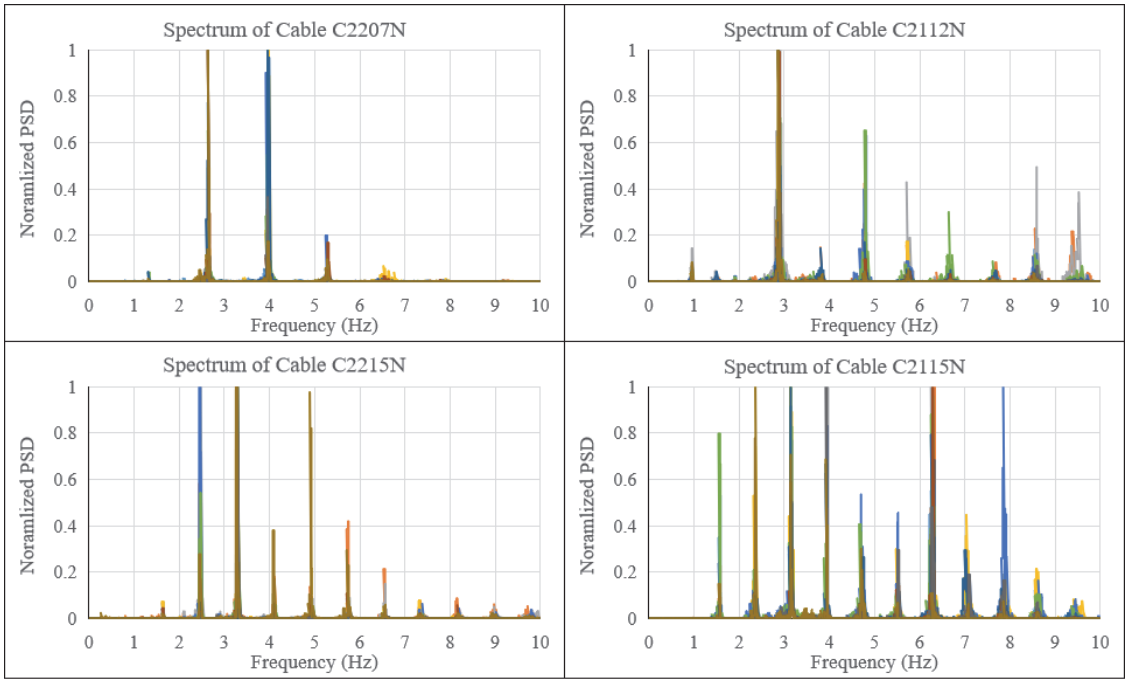

Figure 3: Cable vibration Spectrums of Phu My Bridge in 2017.

In this calculation, Hierarchical Bayes model is adopted since the vibration data of cables are naturally grouped by each cable, measurement session, shape mode, and the sample sizes are sparse and unbalanced across groups. Multiple physical factors act together, such as tension, bending stiffness, boundary, and viscoelastic effects, and often include missing data due to noise or error, additional, a framework is needed to allow group-specific behavior while still sharing information across groups. The hierarchical Bayesian approach allows each group to have its own baseline and sensitivity while still sharing information across groups through partial pooling, which gives more stable estimates and full posterior uncertainty for every parameter, which single regression cannot capture. This statistics model also lets us embed physics in two complementary ways: a phenomenological regression that relates tension to explanatory variables such as the reciprocal of

storage modulus or a viscoelastic factor, and a physics-informed likelihood that predicts frequencies from tension and section properties to infer tension directly. Results are presented with shrinkage plots, trend lines with credible bands, caterpillar plots of group parameters, posterior predictive checks by mode, and fit-metric tables. Another advantage is that it can easily integrate mechanical principles into the statistical framework, linking observed frequencies to underlying physical quantities such as tension and stiffness.

The data analysis followed a clear workflow, with the first step, vibration measurements were organized into a long-format table including cable name, session, measured frequency, and related covariates. Secondly, derived variables such as effective length or viscoelastic factor were calculated, and modes with reliable signals were selected. Third, Bayesian hierarchical models were built with weakly informative priors and fitted using MCMC sampling. Convergence diagnostics ensured the reliability of the posterior estimates. Fourth, posterior summaries and predictive checks were conducted to evaluate model fit. Finally, graphical outputs were generated: shrinkage plots showing per-cable tension estimates, trend plots with 95 to 99% credible bands illustrating global relationships, caterpillar plots for group parameters, and posterior predictive. These visualizations link the statistical inference directly to mechanical interpretation, highlighting the trend and uncertainty in each cable's estimated tension.

Bayesian hierarchical modeling was applied to estimate the posterior distributions of the model parameters and produce cable-specific predictions with credible intervals. Tensile force is taken as the real part of Eqn. (16). Tab. 5 for the model in Eqn. (18) with E' and N across five cables such as: C2102N, C2207N, C2212N, C2215N, and C2115N. The CI99 for the slope b excludes zero, indicating a statistically significant effect at the cable level. Since the predictor is $X=E'$, a positive b means N increases as $1/E'$ increases equivalently, N decreases as E' increases. While intercepts a differ substantially by cable, the slopes, are nearly identical, showing that Eqn. (18) captures a common trend shared by all cables: $1/E'$ has the same influence across cables, and between cable differences are primarily offset rather than differences in sensitivity.

$$N = a + \frac{b}{X} \tag{18}$$

The Fig. 4 shows the relationship between tensile force, N, and the storage modulus, E', with medians and 99% prediction ranges for the data sets C2102N, C2207N, C2212N, C2215N, and C2115N. Tensile force ranges from 6×10^7 N to 13×10^7 N as E' varies from 2×10^{11} 10^{11} Pa to 12×10^{11} Pa, while the 99% prediction range shows some uncertainty, especially at $E'\approx2\times10^{11}$ Pa and above, with some data points falling outside the range. The data sets tend to be similar at $E'\approx6\times10^{11}$ Pa and 8×10^{11} Pa, but C2102N and C2115N have higher tension at some points. Some outliers need to be further considered to improve the accuracy of the prediction model.

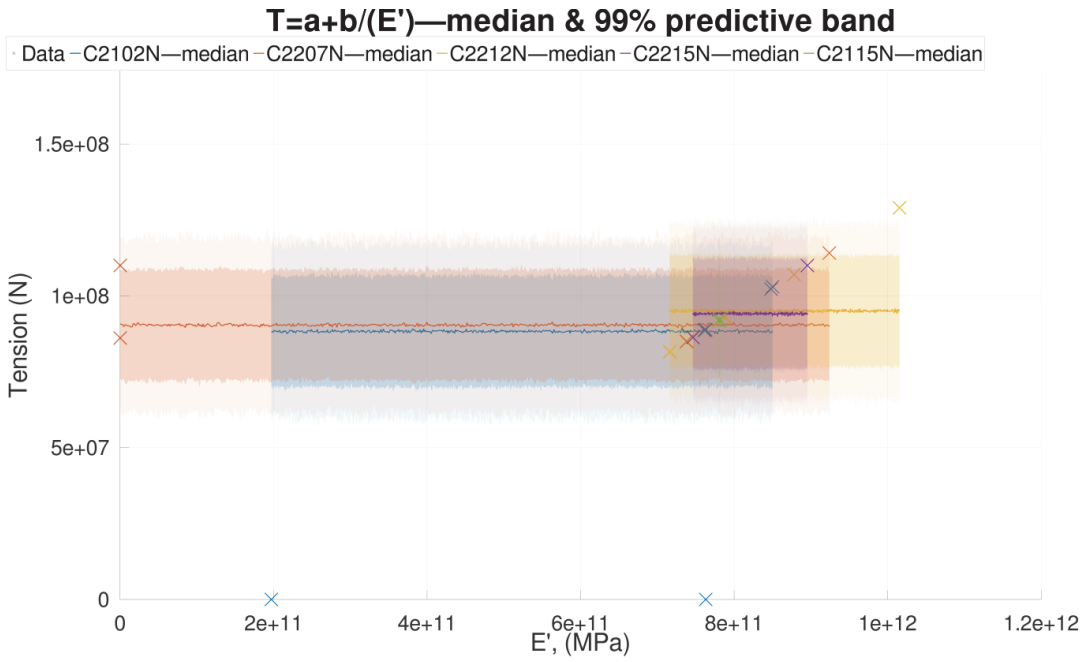

Figure 4: Median and 99% predictive band for storage modulus (E') and tensile force (N).

In Fig. 5, the posterior distribution of μ_a, the global mean of cable-level intercepts, in the model $N=a+b/E'$ was shown with the highest frequency (400; 500) samples centered around zero, symmetrical and decreasing from -4000 to 4000. The distribution is dense at -2000 to 2000, low at the extremes. From Tab. 5, a_{mean} ranges from 88325831 N to 95032006 N between cables, a_{sd} from 8724 N to 73420 N, b_{mean} is stable 652.69 N·Pa (CI99: 476.38 to 932.44). Extreme values (-4000; 4000) are rare exceptions. The model is stable around $\mu_a=0$, but a_{sd} variation like needs further study to increase reliability.

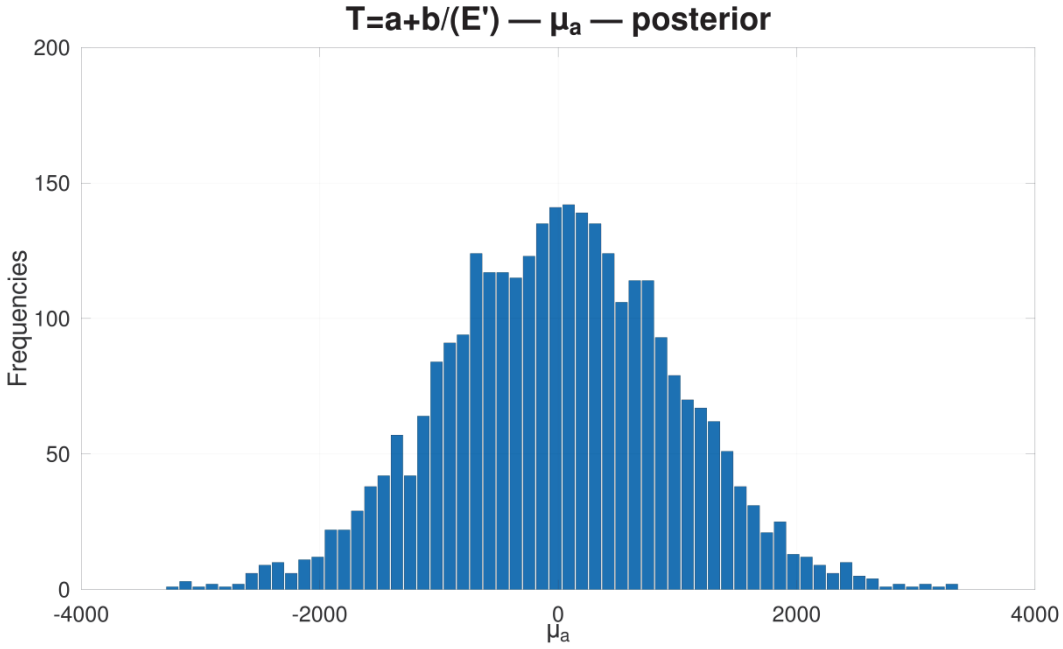

Figure 5: The posterior distribution of mean μ_a for storage modulus (E') and tensile force (N).

Cables	a_{mean}	a_{sd}	a_{CI99}^{low}	a_{CI99}^{high}	b_{mean}	b_{sd}	b_{CI99}^{low}	b_{CI99}^{high}
	N	N	N	N	$N \cdot Pa$	$N \cdot Pa$	$N \cdot Pa$	$N \cdot Pa$
C2102N	88325831	8724	88291125	88338149	652.72	118.48	476.38	932.44
C2207N	90393025	20679	90310783	90422231	652.69	118.48	476.27	932.46
C2212N	95032006	14152	94975713	95051991	652.69	118.51	476.42	932.66
C2215N	94085064	73420	93793444	94188880	652.69	118.51	477.17	932.93
C2115N	91880992.	16900	91813772	91904860	652.69	118.51	476.27	932.84

Table 5: Per cable summary for relationship between storage modulus (E') and tensile force (N).

The graph (Fig. 6) shows the relationship between N and the variable C_a, with medians and 99% prediction ranges for the data sets C2102N, C2207N, C2212N, C2215N, and C2115N. Tensile force ranges from 6×10^7 N to 13×10^7 N as C_a varies from 5.2×10^{11} Pa·s$^{\alpha}$ to 8.3×10^{11} Pa·s$^{\alpha}$. The 99% prediction range (light color) shows large variation at $C_a>7\times10^{11}$ Pa·s$^{\alpha}$, with some data points falling outside the range, possibly outliers. The medians show similarities between the sets, but C2115N tends to be higher at large C_a. Each colored band represents the 99% posterior predictive distribution for one cable, including both parameter uncertainty, and observation-level uncertainty. Because these uncertainties are substantial relative to the differences between cables, bands overlap almost entirely in the central region. Overlap therefore represents: shared predictive ranges, absence of strong cable-to-cable separation, and convergence of all posterior predictions to a common tension interval.

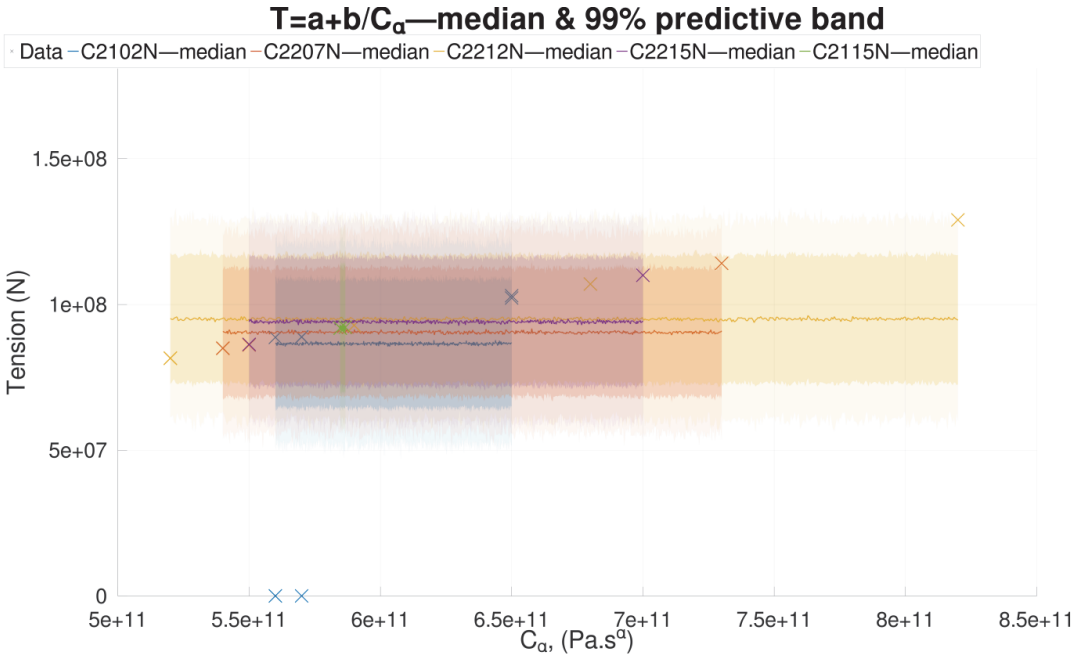

Figure 6: Median and 99% predictive band for damping coefficient (C_a) and tensile force (N).

The posterior distribution of the global mean of cable-level intercepts (μ_a) was shown (Fig. 7), the global mean intercept across cables; its center and width summarize the baseline level and its uncertainty, the posterior under $N=a+b/C_a$ is unimodal, roughly normal, centered near zero with slight left skew, indicating a stable global baseline and no multimodality; the width conveys uncertainty.

The histogram from Fig. 7 shows the posterior distribution of the global mean of cable-level intercepts, μ_a, in this model, with the highest frequency from 400 to 500 centered around zero, symmetrical and decreasing from -4000 to 4000. The distribution is dense at -2000 to 2000, low at the extremes. Tab. 6, a_{mean} ranges from 86523172 N (C2102N) to 94988594 N (C2212N), a_{sd} from 11973 N (C2102N) to 105965 N (C2215N), b_{mean} is stable at 1429.65 N·Pa·s$^{\alpha}$. (CI99: 1284.89; 1687.51). Extreme values (-4000 ; 4000) are rare exceptions.

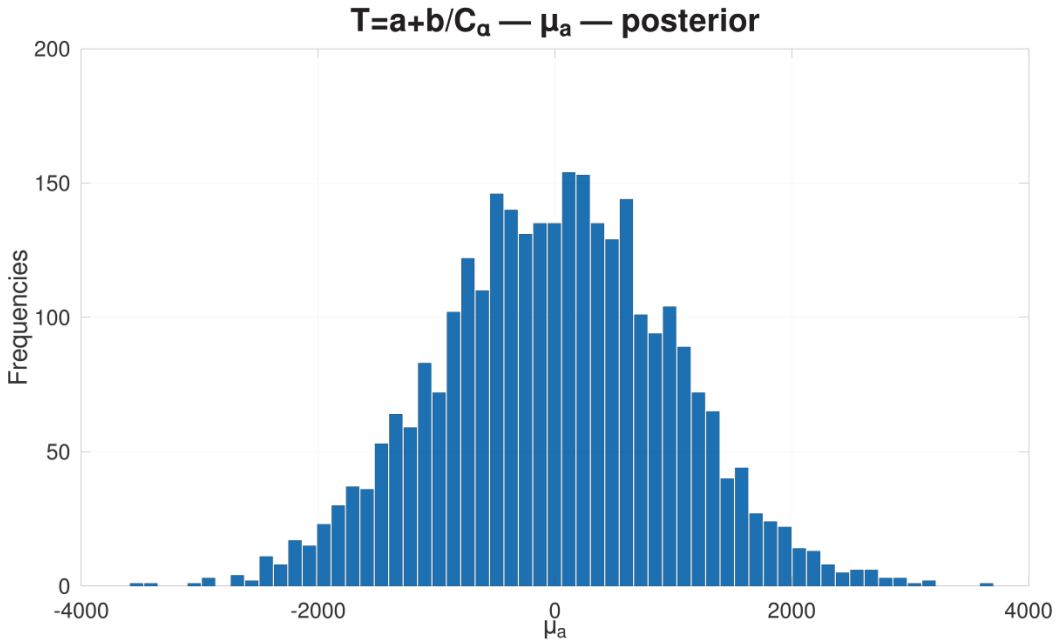

Figure 7: The posterior distribution of mean μ_a for damping coefficient (C_α) and tensile force (N).

Cables	a_{mean}	a_{sd}	a_{CI99}^{low}	a_{CI99}^{high}	b_{mean}	b_{sd}	b_{CI99}^{low}	b_{CI99}^{high}
	N	N	N	N	$N.Pas^{\alpha}$	$N.Pas^{\alpha}$	$N.Pas^{\alpha}$	$N.Pas^{\alpha}$
C2102N	86523172	11973	86478346	86540438	1429.65	110.21	1284.89	1687.49
C2207N	90378017	29877	90266208	90421120	1429.66	110.16	1285.07	1686.81
C2212N	94988594	20123	94913267	95017619	1429.63	110.20	1285.10	1687.25
C2215N	94031804	105965	93635942	94184927	1429.66	110.20	1285.42	1687.51
C2115N	91868727	24419	91777328	91903952	1429.64	110.22	1285.15	1686.35

Table 6: Per cable summary for relationship between damping coefficient (C_a) and tensile force (N).

Also Eqn.18 fits across five cables, slopes b is nearly identical, and these cables have b-CIs excluding zero, indicating significance at the cable level. Intercepts a show CV≈3.65%, reflecting baseline differences by cables. Since b<0, tensile force increases as X=1/C_α increases. We recommend using a common slope with cable-specific a for prediction.
For the Eqn.18 fits across five cables, slopes b is nearly identical as shown in Tab. 7, the relationship between tensile force and frequency in the model $N=a+b/f$, with medians and 99% prediction bands for the C2102N, C2207N, C2212N, C2215N, and C2115N data sets. The cable tension ranges from 6×10^7 N to 13×10^7 N as the natural frequencies f vary from 0 Hz to 14 Hz. The 99% prediction band is wider at low frequencies (<6), narrowing at high frequencies (>10), with a few data points falling outside the band, possibly being outliers. The medians show a similar pattern, but C2115N tends to be higher at high frequencies, tensile force decreases as $X=f$ increases, as shown in Fig. 8.

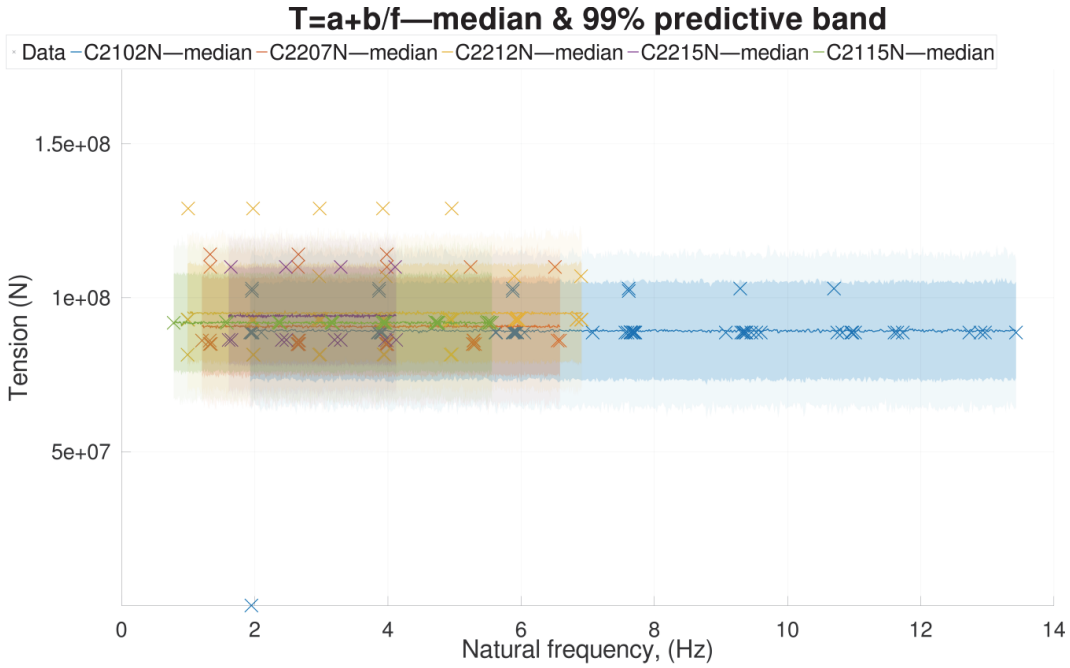

Figure 8: Median and 99% predictive band for frequency (f) and tensile force (N).

According to Fig. 9, the posterior distribution of μ_a was shown with the model $N=a+b/f$, with the highest frequency 400 to 500 centered around zero, symmetrical and decreasing about ±4000.
This posterior is unimodal, roughly normal, centered near zero with slight left skew, indicating a stable global baseline and no multimodality. The distribution is dense at -2000 to 2000, low at the extremes. From Tab. 7, a_{mean} ranges from 89268442 N (C2102N) to 95003595 N (C2212N), a_{sd} from 6700 N (C2102N) to 55256.N (C2215N), b_{mean} is stable at 1153.78 N·Hz (CI99: 872.40; 1502.79).

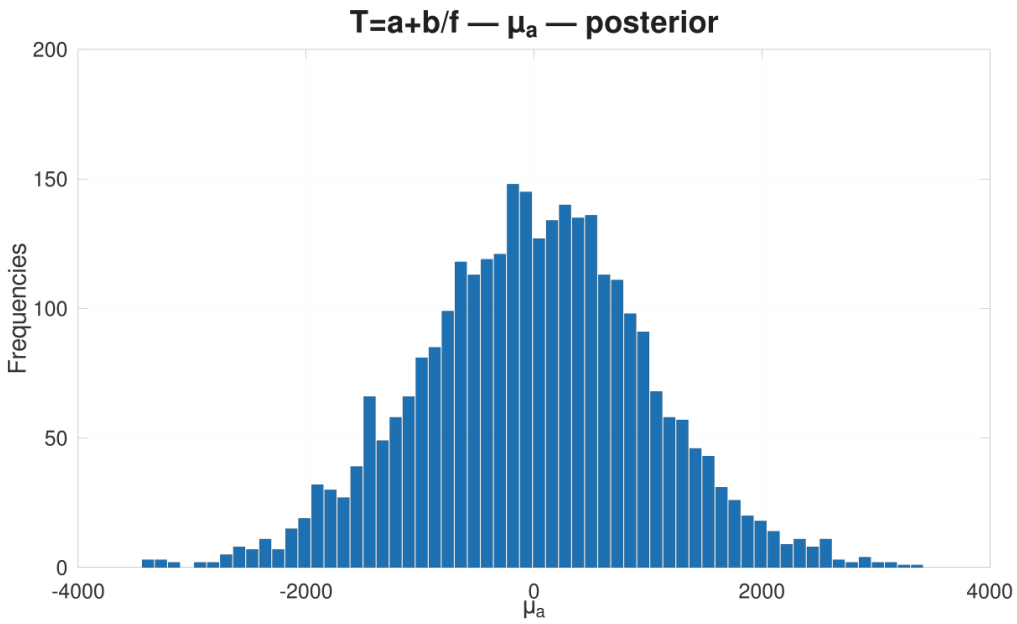

Figure 9: The posterior distribution of mean μ_a for natural frequency (f) and tensile force (N).

Cables	a_{mean}	a_{sd}	a_{CI99}^{low}	a_{CI99}^{high}	b_{mean}	b_{sd}	b_{CI99}^{low}	b_{CI99}^{high}
	N	N	N	N	$N \cdot Hz$	$N \cdot Hz$	$N \cdot Hz$	$N \cdot Hz$
C2102N	89268443	6700	89243787	89278075	1153.78	189.25	872.41	1502.79
C2207N	90680697	16401	90620334	90704288	1153.77	189.26	873.39	1502.57
C2212N	95003595	10473	94965061	95018655	1153.74	189.25	872.40	1502.08
C2215N	94112521	55256	93909215	94191997	1153.74	189.29	872.80	1502.67
C2115N	91887045	12710	91840268	91905325	1153.79	189.24	873.07	1502.78

Table 7: Per Cable Summary for relationship between frequency (f) and tensile force (N).

Fig. 10 shows the relationship between tensile force, N and loss factor, η in model $N=a+b/\eta$, with medians and 99% prediction ranges for data sets C2102N, C2207N, C2212N, C2215N, and C2115N. In Tab. 8, tension ranges from 6×10^7 N to 13×10^7 N as loss factor η varies from 0 to 1.4×10^{-8}. The 99% prediction range (light color) is wider at low loss factor, $\eta<6.0\times10^{-7}$, narrowing at high values, $\eta>1.4\times10^{-8}$ with some data points falling outside the range, possibly being outliers. The medians show similarities across sets, but C2115N tends to be higher at large loss factor.

Cables	a_{mean}	a_{sd}	a_{CI99}^{low}	a_{CI99}^{high}	b_{mean}	b_{sd}	b_{CI99}^{low}	b_{CI99}^{high}
	N	N	N	N	N	N	N	N
C2102N	89264658	6609	89240053	89274104	773.44	228.47	318.34	1079.07
C2207N	90400981	15504	90343271	90423145	773.44	228.47	318.19	1080.04
C2212N	95004059	10440	94965194	95018981	773.44	228.45	318.50	1079.35
C2215N	94113321	55082	93908473	94192131	773.43	228.48	318.52	1079.47
C2115N	91887494	12670	91840329	91905606	773.45	228.49	318.57	1079.39

Table 8: Cable Summary for relationship between loss factor (η)-tensile force (N).

For Eqn. (18), the results fit across five cables, slopes b_{mean} is nearly identical, indicating moderate baseline differences. With $b>0$, tensile force decreases as X increases as shown in Tab. 8.

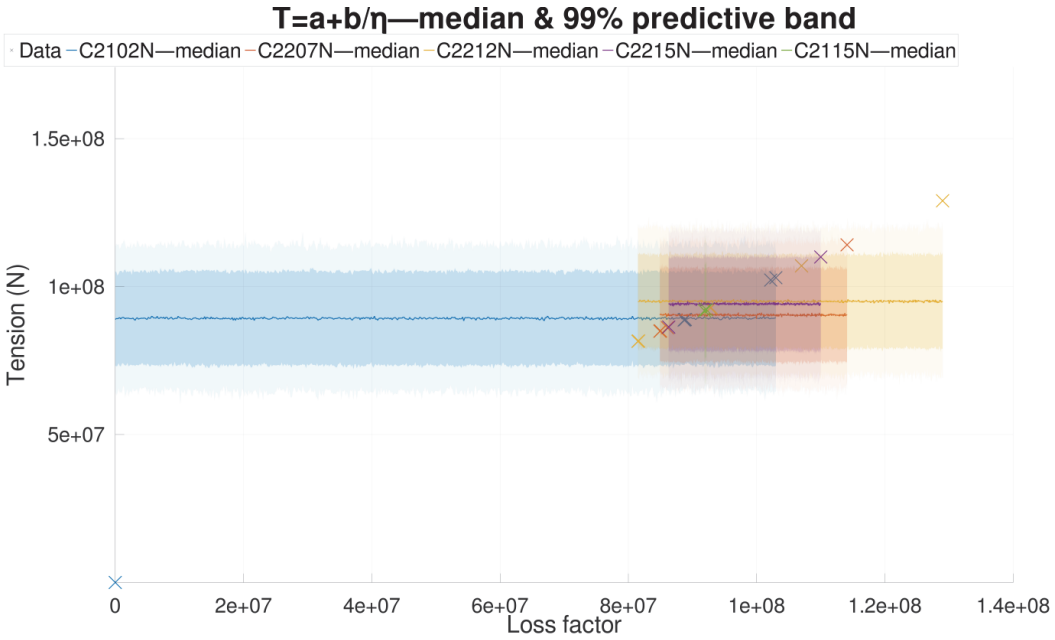

Figure 10: Median and 99% predictive band for loss factor (η)-tensile force (N).

The histogram shows the posterior distribution of μ_a as shown in Fig. 11. The distribution is unimodal and approximately bell-shaped, centered near zero with a slightly heavier left tail. Its smooth, single-peaked shape, consistent with the prior trace plot, indicates good mixing and stationarity. The width encodes the uncertainty in the global mean of the average baseline tensile force across cables. As the model uses Eqn. (18), μ_a corresponds to the baseline as $1/X \to 0$ ($X \to \infty$)); a center near zero implies the global baseline is not strongly shifted in this parametrization. The absence of multiple modes suggests no competing posterior solutions for μ_a.

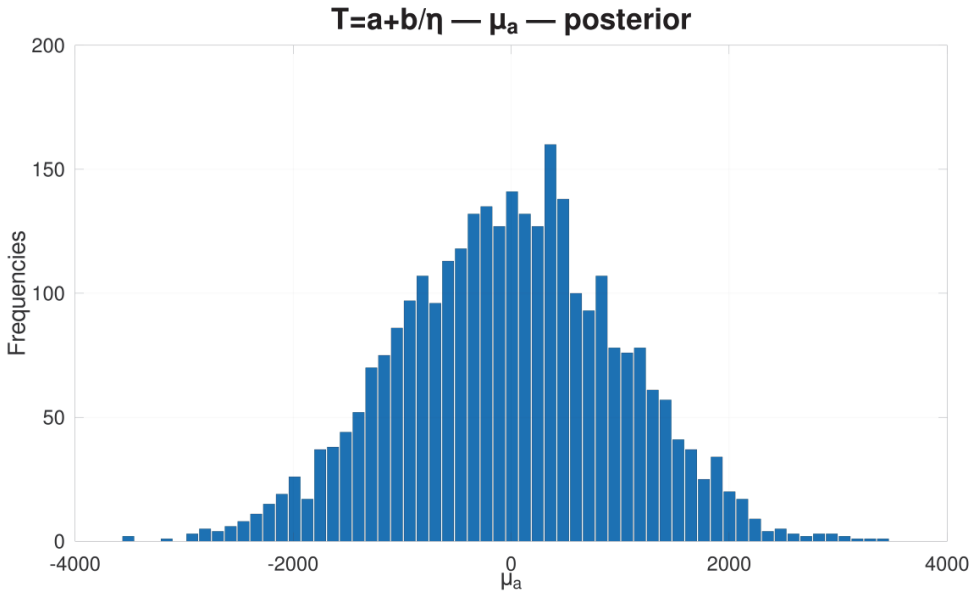

Figure 11: The posterior distribution of mean μ_a for for loss factor (η)-tensile force (N).

The Figs. 6, 8 and 10 present the posterior predictive distribution for the regression model where the shaded regions denote

the 99% predictive bands based on full Bayesian uncertainty. The width of the band reflects both parameter uncertainty and observation-level variability. The relatively large vertical spread indicates that tension inferred from modal data carries substantial uncertainty, likely due to variability in damping estimates or measurement noise. Individual cable data mostly fall inside the band. The observed tensions for cables C2102N, C2207N, C2212N, C2215N, etc., fall largely within the 99% predictive region. This indicates a good overall calibration of the model. The overlapping shaded regions show that tension levels across cables are statistically similar, with no clear outliers once uncertainty is considered. The wide predictive band indicates significant epistemic uncertainty in tension estimation from modal data. The T=a+b/X relationship appears weak, as reflected by the nearly horizontal predictive band. The model adequately predicts most observations, indicating reasonable structural validity. Outlying points may highlight measurement variation or cable-specific behaviour requiring further consideration.

The summary data from Tab. 9 provides the statistical parameters for all the models, based on five cables with the number of observations ranging from 260 to 266. The mean, μ_a ranges around zero (-14.7; -8.2) with a standard deviation, μ_{sd}^{a} of 1000 and a CI99 ranging from -2614 to 2646. The coefficient μ_b varies with the variable 773 for η, 652 for E', 1429 for C_a, 1153 for f, with corresponding CI99s ranging from 318 and 1079 to 873 and 1502. The standard deviation σ ranges from 9645203 N to 13401980 N. A negative association likely exists, but uncertainty remains high due to limited data and an outlier.

Model T	μ_a N	μ_{sd}^{a} N	${}_a\mu_{CI99}^{low}$ N	${}_a\mu_{CI99}^{high}$ N	μ_b $N[X]$	μ_{sd}^{b} $N[X]$	${}_b\mu_{CI99}^{low}$ $N[X]$	${}_b\mu_{CI99}^{high}$ $N[X]$	σ N	σ_{sd} N	${}_\sigma\mu_{CI99}^{low}$ N	${}_\sigma\mu_{CI99}^{high}$ N	N_{obs}
$a+\frac{b}{\eta}$	-10.2	1008.0	-2614.3	2581.9	773.4	228.5	318	1079	9645203	424110	9645203	424110	263
$a+\frac{b}{E'}$	-14.7	1014.7	-2548.4	2646.4	652.7	118.5	476	932	11111557	488110	11111557	488110	262
$a+\frac{b}{f}$	-8.2	1000.5	-2577.8	2610.0	1153.8	189.3	873	1502	9677124	420819	9677124	420819	266
$a+\frac{b}{C_\alpha}$	-14.4	997.0	-2576.5	2592.9	1429.6	110.2	1285	1686	13401980	584110	13401980	584110	260

Table 9: Per model Summary for four models.

According to Fig. 12, the μ_a trace from using MCMC diagnostics for Eqn. (18) variation densely around a stable level with no drift, near-constant amplitude across about 8000 samples, and frequent center crossings, evidence of stationarity and good mixing; no sticking or jumps. This indicates a stable estimate of μ_a, the global meaning of the cable intercepts.

Last but not least, consolidating results so far, all models, the posterior distribution of μ_a is symmetrical around zero, peaks in frequency about 400 to 500, has a thickness around ±2000, and thins out to ±4000; extreme values are rare outliers. The mean values are approximately -10.25, -14.73, -14.38, and -8.16, respectively, all very close to zero with a standard deviation of 1000 ($997 \leq \mu_{sd}^{a} \leq 1014$). The CI99 for μa are almost identical, ranging from -2.6×10^3 to 2.6×10^3. The μ_a is not significantly different from zero in all four models; the choice of predictor variables (η, E', C_a, f) hardly changes the distribution of the intercept. The model is stable around $\mu_a = 0$; further variation needs to be considered.

To summarize this study, a cable tension calculation process is shown in Fig. 13 with the input of geometric parameters, materials from the management unit, collecting vibration measurement signals through the accelerometer, along with pre-processing steps, processing the measurement signals, we can easily obtain the natural oscillation frequency of the cable under operating conditions. Together with the formulas determined in the above section, we obtain the attenuation coefficient, damping coefficient, and cable tension. The Eqn. (18) is used to determine the relationship between the specified quantities and to provide the credible interval for the cable tension value, the posterior formula, and the sample mean of the data set.

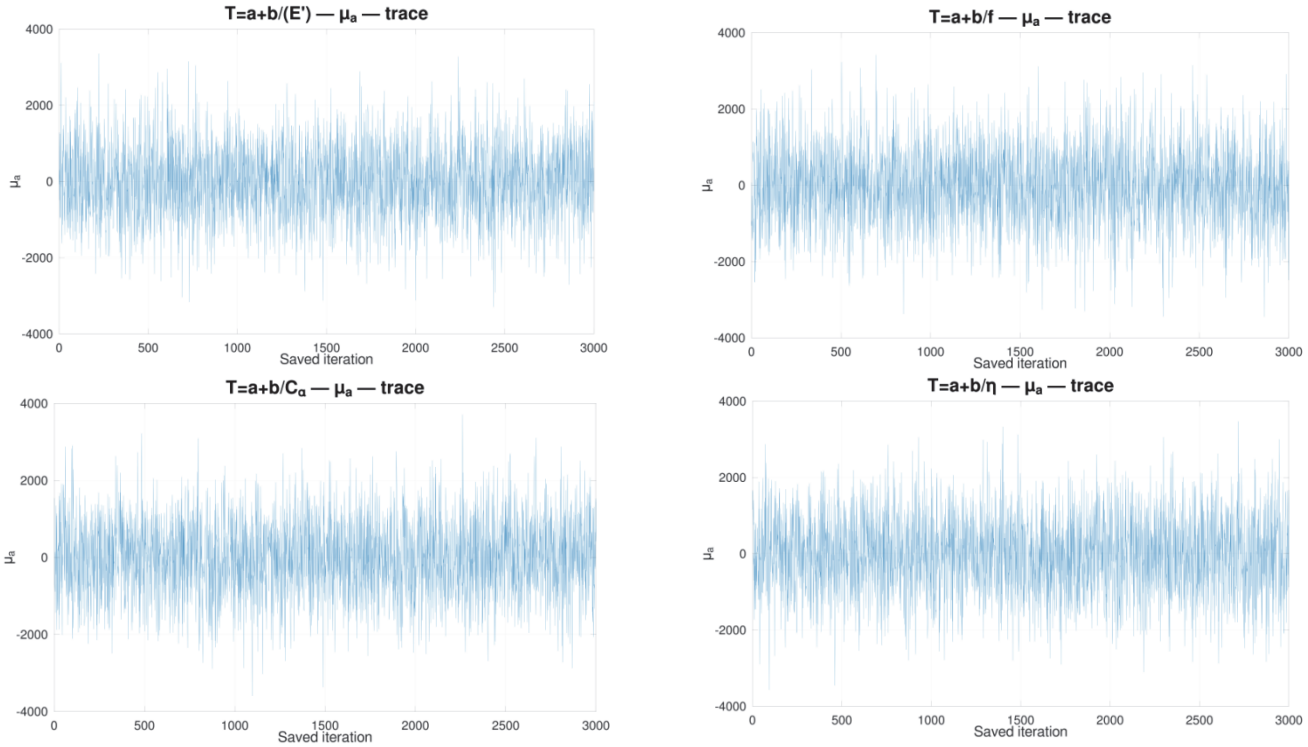

Figure 12: The trace plot of the parameters for the hierarchical Bayes model Eqn.18.

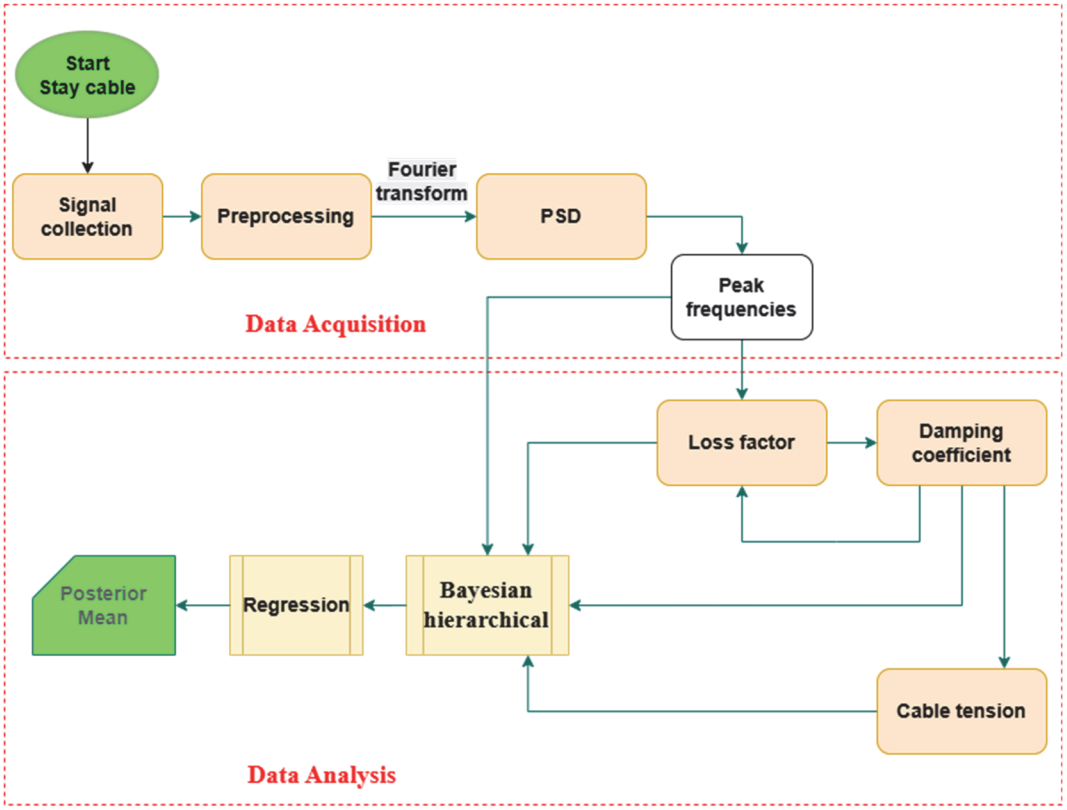

Figure 13: Calculation flowchart of the study.

CONCLUSION

This research confirms that vibration-based tensile force estimation is a practical first-line method for continuous cables, as it is fast, low-cost, and accurate enough for routine inspections of cable structures, such as extradosed, suspension, and cable-stayed bridges, post-tensioned systems, stadiums, and towers. Extending Rayleigh's beam with viscoelastic damping (together with flexural rigidity and mass) and solving the resulting fourth-order ODE enabled indirect estimation of both tensile force and damping from measured frequencies of cables.

Across the Bayesian hierarchical fits Eqn.18 with candidate predictors $X \in (\eta, E', Ca, f)$, a common mechanism was found that cable-level slopes were nearly identical, while most between-cable variation appeared in the intercepts a. Depending on X, the global direction can differ so that tensile force decreases as X increases; and vice versa. For the loss-factor model specifically, the 99% credible interval (CI99) of the global slope included zero, indicating that a global effect was not confirmed, despite the per-cable slopes being precise and consistent. MCMC diagnostics, trace, and posterior of μa showed stationary, unimodal posteriors, indicating stable inference. Use a common slope for each selected predictor and cable-specific intercepts for prediction and monitoring; explicitly model material damping when deriving tensile force from vibration; and prefer predictors that minimize the posterior residual σ and yield well-covering predictive bands. The approach is field-ready, lightweight to run, yet richer than current practice, so it can be embedded in periodic inspections.

Limitations and next study, the form, Eqn.18, may miss mild nonlinearities or omitted covariates (temperature, sag, etc.). Future work should expand the Bayes model, the diagnostics, and formal posterior predictive checks, and compare alternative damping parameterizations.

ACKNOWLEDGEMENTS

This research is funded by Vietnam National University Ho Chi Minh City (VNU-HCM) under grant number C2024-20-02. We acknowledge Ho Chi Minh City University of Technology (HCMUT), VNU-HCM, for supporting this study.

REFERENCES

[1] Shimada, T., Kimoto, K. and Narui, S. (1989). Study on estimating tension of tied hanger ropes of suspension bridge by vibration method. Proc. JSCE, 404(I-11), pp. 455-458. DOI: https://doi.org/10.2208/jscej.1989.404_455 (Japanese).

[2] Shimada, T. (1994). Estimating method of cable tension from natural frequency of high mode. Doboku Gakkai Ronbunshu, 1994(501), pp. 163-171 (Japanese).

[3] Tabatabai, H., Mehrabi, A. B., and Yen, W. H. P. (1998). Bridge stay cable condition assessment using vibration measurement techniques. In Structural Materials Technology III: An NDT Conference, 3400, pp. 194-204. SPIE. DOI: https://doi.org/10.1117/12.300091.

[4] Cho, S., Yim, J., Shin, S. W., Jung, H. J., Yun, C. B., & Wang, M. L. (2013). Comparative field study of cable tension measurement for a cable-stayed bridge. Journal of Bridge Engineering, 18(8), pp. 748-757. DOI: https://doi.org/10.1061/(ASCE)BE.1943-5592.0000421.

[5] Dinh, N. D. T. T. and Hung, N. H. (2020). Evaluating the cable tension results by lift-off and vibration method in Viet Nam. In IOP Conference Series: Materials Science and Engineering, 869(5), p. 052062. IOP Publishing. DOI: https://doi.org/10.1088/1757-899X/869/5/052062.

[6] Jakiel, P., and Mańko, Z. (2017). Estimation of cables' tension of cable-stayed footbridge using measured natural frequencies. In MATEC Web of Conferences, 107, p. 00006. EDP Sciences. DOI: https://doi.org/10.1051/matecconf/201710700006.

[7] Suangga, M., Hidayat, I., and Bontan, D. J. (2017). The analysis of cable forces based on natural frequency. In IOP conference series: earth and environmental science, 109(1), p. 012028. IOP Publishing. DOI: https://doi.org/10.1088/1755-1315/109/1/012028.

[8] Syamsi, M. I., Wang, C. Y., and Nguyen, V. S. (2023). Influence of distance between the first sensor and support in determining tension of fixed-end cable using multiple synchronized vibration measurement. In IOP conference series: earth and environmental science, 1205(1), pp. 012053. IOP Publishing. DOI: https://doi.org/10.1088/1755-1315/1205/1/012053.

[9] Koščo, T., Margetin, M., Chmelko, V., and Šulko, M. (2024). Bridge cable tension estimation using the vibration method. Structures, 63, p. 106332. Elsevier. DOI: https://doi.org/10.1016/j.istruc.2024.106332.
[10] da Costa Azevêdo, A. S., and dos Santos Hoefel, S. (2015). Modal analysis for free vibration of four beam theories, Proceedings of the 23rd International Congress of Mechanical Engineering-COBEM, 2015. DOI: https://doi.org/10.20906/CPS/COB-2015-0991.
[11] da Costa Azevêdo, A. S., and dos Santos Hoefel, S. (2016). Analysis of Rotatory Inertia and Shear Deformation on Transverse Vibration of Beams. In Congresso Nacional de Engenharia Mecanica (CONEM), pp. 21-25. DOI: https://doi.org/10.20906/CPS/CON-2016-1101.
[12] Nathaniel, O. S., and Alimi, A. (2017). on the dynamic behavior of uniform rayleigh beam with an acceleratinf distributed mass, 2017-04, American Journal of Innovative Research and Applied Sciences, 4(4), pp. 136-143.
[13] Yang, M., Hu, Y., Zhang, J., Ding, G., and Song, C. (2018). Analytical model for flexural damping responses of CFRP cantilever beams in the low-frequency vibration. Journal of Low Frequency Noise, Vibration and Active Control, 37(4), pp. 669-681. DOI: https://doi.org/10.1177/1461348418756024.
[14] Zhu, K., and Chung, J. (2019). Vibration and stability analysis of a simply-supported Rayleigh beam with spinning and axial motions. Applied Mathematical Modelling, 66, pp. 362-382. DOI: https://doi.org/10.1016/j.apm.2018.09.021
[15] Rossikhin, Y. A., and Shitikova, M. V. (2018). The fractional derivative Kelvin–Voigt model of viscoelasticity with and without volumetric relaxation. In Journal of Physics: Conference Series, 991(1), p. 012069. IOP Publishing. DOI: https://doi.org/10.1088/1742-6596/991/1/012069.
[16] Xu, Y., Zhang, J., Zhang, Y., and Li, C. (2022). A novel approach for cable tension monitoring based on mode shape identification. Sensors, 22(24), p. 9975. DOI: https://doi.org/10.3390/s22249975.
[17] Van Khang, N., Phuong, N. M., and Chung, P. T. (2022). Forced transverse vibrations of fractional viscoelastic Euler-Bernoulli beam using the modal analysis method. Vietnam Journal of Science and Technology, 60(1), pp. 127-139. DOI: https://doi.org/10.15625/2525-2518/15861.
[18] Łabędzki, P. (2025). Fractional Kelvin–Voigt Model for Beam Vibrations: Numerical Simulations and Approximation Using a Classical Model. Electronics, 14(10), p. 1918. DOI: https://doi.org/10.3390/electronics14101918.
[19] Le, L. X., Siringoringo, D. M., Katsuchi, H., and Fujino, Y. (2022). Stay cable tension estimation of cable-stayed bridge under limited information on cable properties using artificial neural networks. Structural Control and Health Monitoring, 29(10), e3015. DOI: https://doi.org/10.1002/stc.3015.
[20] Furukawa, A., Hirose, K., and Kobayashi, R. (2022). Tension estimation method for cable with damper and its application to real cable-stayed bridge. In Experimental Vibration Analysis for Civil Engineering Structures: Select Proceedings of the EVACES 2021, pp. 379-390. Cham: Springer International Publishing. DOI: https://doi.org/10.1007/978-3-030-93236-7_32.
[21] Furukawa, A., Sugimachi, Y., and Takeichi, T. (2024). Development of tension estimation method without damper modeling error for cable with damper. Structural Monitoring and Maintenance, 11(2), pp. 127-148. DOI: https://doi.org/10.12989/smm.2024.11.2.127.
[22] Nguyen, D. T., Chau, S. Q., and Phan, H. N. (2024). Damping effects of a stay cable attached with a viscous damper and a high damping rubber damper considering cable bending stiffness and damper support flexibility. Advances in Bridge Engineering, 5(1), 12. DOI: https://doi.org/10.1186/s43251-024-00123-7.
[23] Farno, E., Baudez, J. C., and Eshtiaghi, N. (2018). Comparison between classical Kelvin-Voigt and fractional derivative Kelvin-Voigt models in prediction of linear viscoelastic behaviour of waste activated sludge. Science of the Total Environment, 613, pp. 1031-1036. DOI: https://doi.org/10.1016/j.scitotenv.2017.09.206.
[24] Bagley, R. L., and Torvik, P. J. (1983). A theoretical basis for the application of fractional calculus to viscoelasticity. Journal of rheology, 27(3), 201-210. DOI: https://doi.org/10.1122/1.549724.
[25] Sedehi, O., Papadimitriou, C., and Katafygiotis, L. S. (2020). Data-driven uncertainty quantification and propagation in structural dynamics through a hierarchical Bayesian framework. Probabilistic Engineering Mechanics, 60, 103047. DOI: https://doi.org/10.1016/j.probengmech.2020.103047.